Enhanced ferrimagnetism in auxetic $NiFe_2O_4$ in the crossover to the ultrathin-film limit

Michael Hoppe,[1] Sven Döring,[1] Mihaela Gorgoi,[2] Stefan Cramm,[1] and Martina Müller[1,3,*]

[1]*Peter Grünberg Institut (PGI-6) and JARA Jülich-Aachen Research Alliance, Forschungszentrum Jülich GmbH, 52425 Jülich, Germany*

[2]*Helmholtz-Zentrum Berlin für Materialien und Energie GmbH, 12489 Berlin, Germany*

[3]*Fakultät für Physik, Universität Duisburg-Essen, 47048 Duisburg, Germany*

(Received 3 November 2014; revised manuscript received 27 January 2015; published 24 February 2015)

We investigate the sensitive interplay between magnetic, electronic, and structural properties in the ferrimagnetic oxide $NiFe_2O_4$. Emphasis is placed on the impact of reduced dimensionality in the crossover from bulk-like to ultrathin films. We observed an enhanced saturation magnetization M_S for ultrathin $NiFe_2O_4$ films on Nb-$SrTiO_3$ (001) substrates that co-occurs with a reduced out-of-plane lattice constant under compressive in-plane epitaxial strain. We found a bulk-like cationic coordination of the inverse spinel lattice independent of the $NiFe_2O_4$ film thickness, thus ruling out a cationic inversion that nominally could account for an enhanced M_S. Moreover, our study instead uncovers a reduction of the unit cell volume, i.e., an auxetic behavior in ultrathin $NiFe_2O_4$ films.

DOI: 10.1103/PhysRevB.91.054418 PACS number(s): 75.47.Lx, 75.50.Gg, 75.70.Ak, 79.60.Dp

I. INTRODUCTION

The competition of charge, spin, and orbital degrees of freedom in complex oxides leads to intriguing physical phenomena, including ferromagnetism, ferroelectricity, and multiferroicity [1]. Fertilized by the continuously advancing art of oxide growth, the controlled synthesis of high-quality oxide heterostructures now approaches a monolayer precision [2]. Designing electronic properties in ultrathin oxide films and interfaces thereby opens up routes to explore novel nanoelectronic functionalities for applications.

In the context of spin-based electronics, oxides featuring both magnetic and insulating properties reveal a highly effective spin-filter effect, where spin-polarized electron currents are generated by a spin-dependent tunneling process. Up to 100% spin filtering has been demonstrated in magnetic oxides with low Curie temperature T_c, such as the binary rare-earth compounds EuO or EuS [3,4], and hence their integration as model spin-injection or -detection contacts to silicon was explored recently [5,6]. Implementing the spin-filter functionality of magnetic insulators in all-oxide heterostructures can extend the scope of applications further towards a multifunctional oxide-based spin electronics.

It is in this pursuit that ferrite materials are envisioned as high-T_c spin filters with the ultimate goal to realize efficient spin filtering for application at room temperature. For example, $NiFe_2O_4$ shows ferrimagnetic ordering up to T_C = 865 K [7] and grows epitaxially on Nb-doped $SrTiO_3$ (001) perovskite electrodes [8,9]. Its inverse spinel lattice of the type $Fe^{3+}[Ni^{2+}Fe^{3+}]O_4$, however, exhibits a high structural complexity: Ni^{2+} cations are situated on octahedrally (O_h) coordinated lattice sites, while Fe^{3+} cations are equally distributed across both tetrahedral (T_d) and O_h sites (Fig. 1). The electronic and magnetic properties of spinel ferrites thus sensitively depend on the details of the interatomic coordinations. In particular, magnetic ordering is dominated by superexchange interactions between T_d- and O_h-coordinated cations on two antiferromagnetically coupled sublattices.

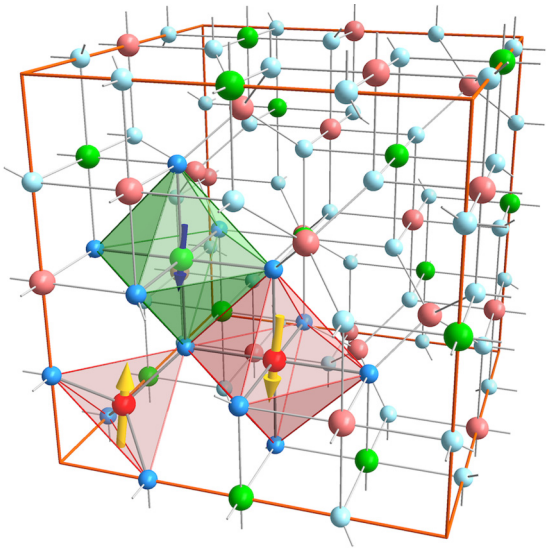

FIG. 1. (Color online) Schematic representation of the inverse spinel lattice of $NiFe_2O_4$: Fe^{3+} cations (red) are distributed equally across tetra- (T_d) and octahedral (O_h) lattice sites, while Ni^{2+} cations (green) occupy O_h sites. An antiferromagnetic coupling between the T_d and O_h sites compensates the magnetic moments of the Fe^{3+} cations, which is why only the Ni^{2+} cations account for the net macroscopic magnetization of 2 μ_B/f.u. (where f.u. denotes formula units).

A structural inversion from the inverse to the normal spinel lattice consequently alters the cationic coordination, as quantified by the inversion parameter λ. Hereby, λ is the fraction of divalent cations occupying O_h sites, with $\lambda = 0$ denoting a normal ($Ni^{2+}[Fe^{3+}Fe^{3+}]O_4$) and $\lambda = 1$ an inverse ($Fe^{3+}[Ni^{2+}Fe^{3+}]O_4$) spinel lattice. In previous studies, an unexpected magnetic behavior, i.e., an enhanced saturation magnetization, was reported for $NiFe_2O_4$ films in the ultrathin-film limit [10,11]. The origin of this phenomenon was explained by a cationic inversion from an inverse to a partly normal spinel lattice ($0 < \lambda < 1$), since this structural redistribution of Fe cations nominally accounts for an increased magnetic moment. Theoretical considerations based

*mart.mueller@fz-juelich.de

on density functional theory calculations find a partial cationic inversion energetically favorable for $NiFe_2O_4$ films under tensile, but not under compressive, strain [12], as is the case for $NiFe_2O_4$ grown on Nb-$SrTiO_3$ (001). The origin of the altered magnetic exchange interaction in ultrathin $NiFe_2O_4$ films thus still remains an open question.

In this work, we explore the details of the electronic and magnetic properties of single-crystalline $NiFe_2O_4$ films in the crossover from bulk-like to the ultrathin-film limit. The goal of our studies is to uncover modifications of the structural, electronic, and magnetic properties with regard to the reduced film dimensionality. We performed a complementing spectroscopic analysis employing the bulk- and surface-sensitive photon spectroscopy techniques hard x-ray photoelectron spectroscopy (HAXPES), x-ray absorption near-edge structure (XANES), and x-ray magnetic circular dichroism (XMCD), respectively, which allow for a precise quantification of the element-specific cationic valencies and spatial coordinations. From our thorough analysis, we can conclude on the absence of a cationic inversion for all $NiFe_2O_4$ film thicknesses. Instead, we find an auxetic behavior of ultrathin $NiFe_2O_4$ films, i.e., a reduction of the unit cell volume, which may correlate to the finding of an enhanced M_S.

II. EXPERIMENTAL DETAILS

A series of $NiFe_2O_4$ thin films with varying thicknesses between 2 and 20 nm has been deposited from stoichiometric targets on conductive 0.1% Nb-doped $SrTiO_3$(001) substrates by utilization of the pulsed-laser deposition (PLD) technique. The substrates were previously etched in buffered hydrofluoric acid to provide a TiO_2-terminated terrace surface [13]. During growth, the laser fluence was set to 1.5 J/cm^2 and a repetition rate of 2 Hz. The oxygen pressure was kept at 0.04 mbar and the substrate was heated to $T_S = 635$°C. After deposition, the samples were postannealed at T_S for 90 min in vacuum.

The thickness of the grown films was determined by x-ray reflectivity (XRR) measurements, while the structural characterization was accomplished by x-ray diffraction (XRD) experiments. Both XRR and XRD experiments were performed on a Philips XPert Materials Research Diffractometer using Cu $K\alpha$ radiation. Bulk magnetic properties of the samples were investigated on a Quantum Design MPMS SQUID. Hysteresis loops were recorded at $T = 5$ K with a magnetic field up to 3.6 T, which was applied parallel to the in-plane [100] axis of the films.

HAXPES experiments were conducted on the HIKE end station of the KMC-1 beam line at the BESSY-II electron storage ring (HZB Berlin) [14]. In contrast to soft x-ray photoelectron spectroscopy, HAXPES experiments use high-energy x-rays with photon energies E_P ranging from 2 to 15 keV. Thus, the kinetic energy as well as the inelastic mean-free path of the emitted photoelectrons are strongly enhanced, which gives HAXPES an information depth (ID) of several tens of nanometers, allowing one to probe the chemical properties of a multilayered film structure with true bulk sensitivity [15]. All spectra shown in this work were taken at $E_P = 4$ keV and at room temperature. The x-ray beam was aligned at 3° grazing incidence and the photoelectron detector normal to the sample surface. The information depth ID(95) is defined as the probing depth from which 95% of the photoelectrons originate and can be estimated by [16]

$$\mathrm{ID}(95) = -\lambda_{\mathrm{IMFP}} \cos\alpha \ln(1 - 95/100), \quad (1)$$

where α denotes the off-normal emission angle and λ_{IMFP} the inelastic mean-free path of the electrons. The values for λ_{IMFP} have been determined using the software SESSA [17] and the given experimental parameters result in an ID(95) $\approx$ 15 nm. The value has to be corrected for elastic scattering, but for the given experimental geometry and photoelectron energies the error is $<1\%$ and thus can be neglected.

XANES experiments were performed at the HIKE end station as well. To record the XANES spectra, the x-ray absorption of the samples was determined by the emitted fluorescence (FY), which was detected by an energy dispersive detector. In contrast, the absorption of the $NiFe_2O_4$ bulk target material was determined in total electron yield (TEY) mode. All signals were normalized to the incident x-ray flux, monitored by an ionization chamber in front of the sample. The incident beam was polarized parallel to the plane of incidence and we found no dependence of the angle between the incident x-ray beam and the sample surface on the resulting normalized spectrum. Thus, the angle was optimized for every spectrum in order to maximize the fluorescence signal without saturating the detector.

For all photon energies used during the HAXPES and XANES experiments, photoemission spectra of the Au 4f core level from an Au reference sample attached to the manipulator have been recorded. The energy position of the Au 4f lines was compared to standard values and all measured data corrected accordingly.

XMCD data were determined by x-ray absorption spectroscopy (XAS) experiments performed at the UE56-1 SGM beam line at BESSY-II. The sample surfaces were aligned in 20° grazing incidence. A magnetic field of 300 mT was applied parallel to the surface and in the plane spanned by the incident beam with the surface normal axis. The absorption signal was taken in TEY mode and was normalized to the incident x-ray flux. The XMCD asymmetry spectra were determined from the difference of two spectra collected by changing the magnetic field to the opposite direction, or by two spectra recorded by changing the polarization from left to right handed. In total, at least four absorption spectra were taken for every sample, each with a different combination of polarization and magnetization direction.

For XMCD data analysis, we have calculated model XMCD spectra using the program CTM4XAS 5.5 [18], which is based on crystal field multiplet calculations including charge transfer effects [19–21]. Using the parameters from Ref. [22], the interatomic screening is taken into account by reducing the Slater integrals F(dd), F(pd), and G(pd) with scaling factors F(dd) = 0.7, F(pd) = 0.8, and G(pd) = 0.8. For octahedral (tetrahedral) symmetry, the crystal field was set to 10 Dq = 1.2 eV (−0.6 eV) and the exchange field was set to M = 10 meV (−10 meV). The resulting spectra were broadened by a Lorentzian width with a half-width of 0.3 eV (0.5 eV) for the L_3 (L_2) edge to respect the core-hole lifetime broadening, and by a Gaussian width of 0.2 eV to account for instrumental broadening.

III. RESULTS

A. Structural and magnetic characterization

First, the thickness-dependent structural properties of ultrathin $NiFe_2O_4$ films on Nb-$SrTiO_3$ (001) were investigated by x-ray diffraction experiments. θ-2θ scans ranging from $2\theta = 20^\circ$ to 100° with a scattering vector parallel to the surface normal were used to analyze the crystalline structure of the films and to confirm their epitaxial growth. All scans show the expected reflections of a (001)-oriented $SrTiO_3$ crystal, as well as two additional reflections at $2\theta \approx 43^\circ$ and $2\theta \approx 95^\circ$, which can be attributed to the $NiFe_2O_4$ (004) and (008) reflections. Since no other reflections are observed, we conclude that the $NiFe_2O_4$ films grow textured along the (001) direction without any parasitic phases. Φ scans around the $SrTiO_3$ (202) and $NiFe_2O_4$ (404) peaks both show a fourfold symmetry and provide evidence that the films grow cube-on-cube on the $SrTiO_3$ substrate, despite the induced biaxial compressive strain of 6.4%. In Fig. 2, the details of the θ-2θ scans around the $NiFe_2O_4$ (004) reflection are shown, which reveal that for decreasing film thickness the center of the $NiFe_2O_4$ (004) peak shifts towards larger angles, implying a decreasing out-of-plane lattice constant a_{oop}. The broadening of the peaks for thinner films is due to the smaller amount of material that contributes to coherent diffraction. For film thicknesses greater than 6 nm, a_{oop} is slightly larger than the bulk value ($a_{bulk} = 8.339$ Å). In combination with the compressive in-plane stress induced by the substrate, this finding reveals the tendency of the material to preserve its bulk unit cell volume. On the other hand, for lower thicknesses a_{oop} decreases, as compiled in the inset of Fig. 2. This refers to a reduction of the unit cell volume for ultrathin films in comparison to the bulk value, a result that also has been reported for $CoFe_2O_4$ films on $SrTiO_3$ [23]. In contrast to $CoFe_2O_4$, however, a_{oop} of $NiFe_2O_4$ even drops below its bulk value for ultrathin films, which implies that $NiFe_2O_4$ shows an auxetic behavior, i.e., a negative Poisson ratio ν in the crossover to the monolayer regime.

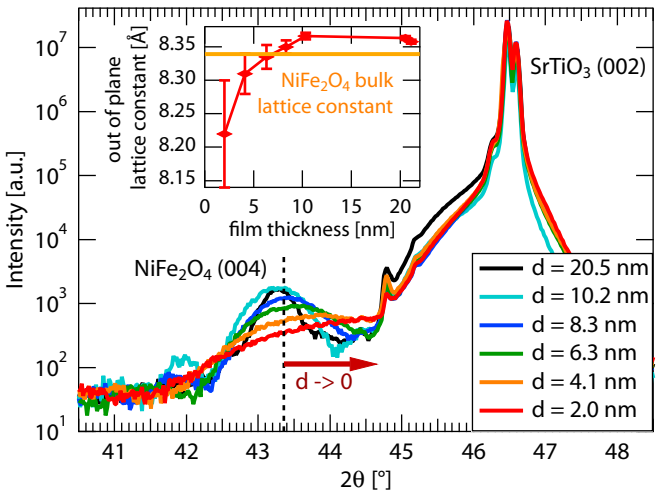

FIG. 2. (Color online) θ-2θ scans of the $NiFe_2O_4$ (004) reflection for varying film thickness. The out-of-plane lattice constant a_{oop} decreases below the bulk value for ultrathin films (see inset).

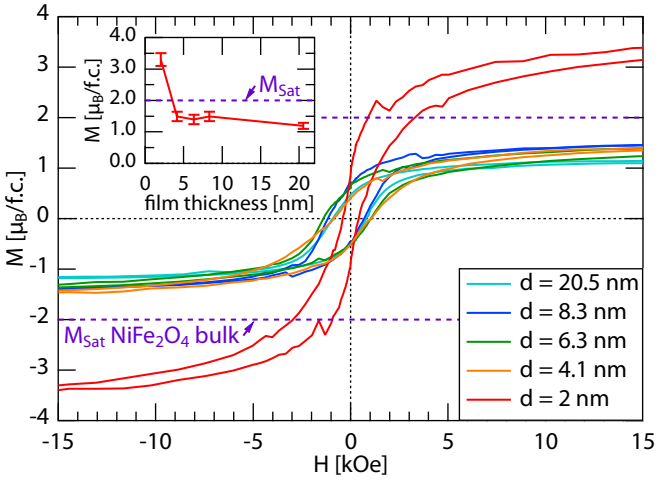

FIG. 3. (Color online) Details of the in-plane M-H hysteresis loops of $NiFe_2O_4$ on $SrTiO_3$ (001) recorded at $T = 5$ K with a maximum applied field of up to 36 kOe. The inset shows the saturation magnetization M_S as a function of $NiFe_2O_4$ film thickness.

Next, the $NiFe_2O_4$ films were investigated with regard to their magnetic properties. Hereby, special attention is paid to changes dependent on their film thickness. Hysteresis loops of all samples were recorded at $T = 5$ K, which are dominated by the diamagnetic contribution of the $SrTiO_3$ substrate. To extract the magnetic response of the $NiFe_2O_4$ films, a subtraction of the diamagnetic background is required. Therefore, linear slopes have been fitted to the high-field tails of the raw signal and subtracted afterwards.

In Fig. 3, details of the hysteresis loops after background correction are depicted, which confirm ferrimagnetic behavior for all $NiFe_2O_4$ film thicknesses. The coercive fields are approximately constant for thicknesses above $d = 6$ nm, but dramatically decrease for $d = 2$ nm. For $CoFe_2O_4$ on MgO, this effect has been interpreted as a result of the reduction of the magnetic anisotropy for thin films [24]. $NiFe_2O_4$ films with thicknesses above 6 nm show a saturation magnetization of $M_S \approx 1.3-1.5\,\mu_B$/f.u., which is lower than the bulk value of $2\,\mu_B$/f.u. [7]. These deviations are supposed to be related to structural dislocations, which form due to the strain incorporated by the substrate, and to the formation of antiphase boundaries during growth. The latter occur due to island forming at different positions on the substrate, which are shifted by half of a unit cell to each other and thus lose periodicity upon merging [25]. This model is supported by the high external magnetic fields required to drive the films into saturation, which is even at 15 kOe not completely accomplished. More striking, when the film thickness scales below 6 nm, we find the saturation magnetization enhancing up to 3 μ_B/f.u.—thus significantly exceeding the bulk value. This result is in agreement with previous studies on $NiFe_2O_4/SrTiO_3$ [10] and $CoFe_2O_4/SrTiO_3$ [26]. So far, this phenomenon was explained in terms of a cationic inversion, where the inverse spinel structure of the bulk state partly changes to a normal spinel structure in the crossover to the ultrathin-film limit. An experimental proof for this model is, however, still lacking.

Moreover, for the thinner films, the contributions from contaminations to the total signal increase. Foerster *et al.* [27] discussed the influence of the substrate, for which in the case of $NiFe_2O_4$ films on $MgAl_2O_4$ the observed increased magnetization can be explained by a paramagnetic contribution from the substrate, which even disappears if the magnetic response of the substrate is subtracted properly. Similar observations have been made in Fe_3O_4, where initially an enhanced magnetization has been attributed to noncompensated cations at the interfaces [28]. But again, the effect was later explained by Fe impurities in the used MgO substrates [29]. Yet, this cannot explain the findings for $NiFe_2O_4$ on $SrTiO_3$, since $SrTiO_3$ shows a purely diamagnetic response and thus validates the applied background subtraction.

In order to evidence the existence or absence of a cationic inversion, we investigate the chemical properties and cationic distribution of $NiFe_2O_4$ as a function of the film thickness in more detail.

B. HAXPES

In a first step, we need to clarify whether the chemical properties of $NiFe_2O_4$ differ for bulk-like and ultrathin films. HAXPES measurements have been performed to quantify the valence states of each cation species. In contrast to soft x-ray photoemission, HAXPES allows us to identify these properties not only at the surface but with bulk sensitivity. The increased information depth even allows us to record reference spectra of the pressed $NiFe_2O_4$ powder used as bulk target for PLD deposition, which does not possess a flat surface as typically required for low-energy photoemission experiments.

Figure 4 plots the Ni $2p$ and Fe $2p$ core level spectra for $NiFe_2O_4$ films of 8 to 2 nm and compares them to the bulk reference. In Fig. 4(a), all spectra of the Ni $2p$ core level display the Ni $2p_{3/2}$ and Ni $2p_{1/2}$ peaks at a binding energy of 855.1 and 872.4 eV, respectively, without a chemical shift relative to the bulk material. The two main peaks are both accompanied by satellite peaks at 7 eV above their binding energies and overlap with the Fe $2s$ core level at lower energies. The shape of all spectra is comparable to that of a single monolayer of NiO [30]; in particular there is no shoulder visible at the high-energy side of Ni $2p_{3/2}$. The occurrence of such a shoulder $\sim$1.5 eV above the $2p_{3/2}$ peak [see NiO bulk reference in Fig. 4(a) for comparison] has been theoretically described by a screening effect that emerges from electrons not originating from the oxygen orbitals around the excited Ni cation, but from adjacent NiO_6 clusters [32]. The HAXPES experiment thus confirms that no NiO clusters have formed within the $NiFe_2O_4$ films. Moreover, the spectra do not show any contribution of metallic Ni^0, which would peak at around 852.8 eV. We therefore conclude that the $NiFe_2O_4$ films contain completely oxidized and homogeneously distributed Ni^{2+} cations only without any NiO cluster formation.

Figure 4(b) depicts the HAXPES data of the Fe $2p$ core levels from all $NiFe_2O_4$ samples with $d = 8$ to 2 nm. For comparison, also model spectra of Fe cations in the inverse spinel structure of magnetite (Fe_3O_4) are given (reproduced from Ref. [31]). These spectra have been calculated individually for the different possible Fe cation lattice site occupancies (O_h, T_d) and valencies (2+, 3+). The Fe $2p_{3/2}$ and $2p_{1/2}$

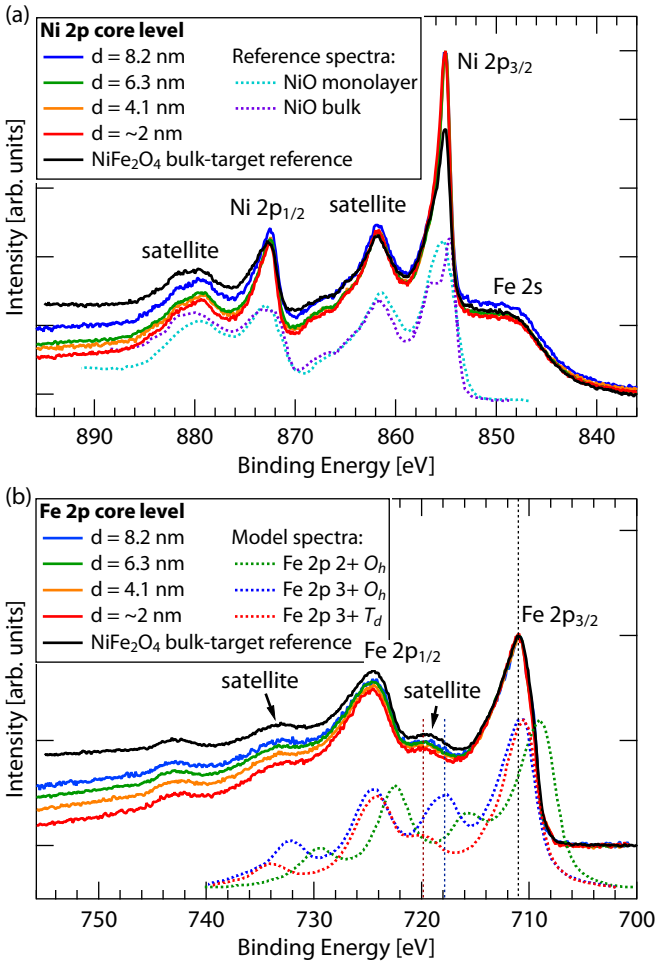

FIG. 4. (Color online) HAXPES spectra of $NiFe_2O_4$ films with varying film thickness recorded at a photon energy of $h\nu = 4$ keV. (a) Ni $2p$ core level spectra and references for one monolayer NiO and NiO bulk [30]. (b) Fe $2p$ core level spectra in comparison to model spectra taken from Ref. [31].

core levels are peaking at binding energies of 710.9 and 724.4 eV, in agreement with the spectrum of the $NiFe_2O_4$ bulk reference and consistent with the literature [33]. The formation of underoxidized Fe^{2+} ions during film growth would result in a characteristic shoulder at the low-energy side of the Fe $2p_{3/2}$ peak due to a chemical energy shift (as observable in the Fe^{2+} O_h reference). All measured spectra coincide with the bulk reference sample, thus confirming that the $NiFe_2O_4$ films consist of fully oxidized Fe^{3+} cations and that the amount of underoxidized Fe^{2+} cations is below the detection limit.

Comparing the Fe^{2+} O_h, Fe^{3+} O_h, and Fe^{3+} T_d model spectra reveals that the main peak binding energies are sensitive to the oxidation state but not to the atomic site occupancy. In contrast, the Fe $2p_{3/2}$ satellite observable between the spin-orbit split Fe $2p$ peaks is caused by a screening effect of the surrounding oxygen ions and deviates significantly for T_d and O_h cation coordination. Thus, its shape and binding energy position can serve as a fingerprint for the chemical state of different iron oxides and the cationic lattice site occupancies [31]. A complete inversion to the normal spinel structure would shift the satellite's spectral

weight to lower binding energies by about 0.8 eV. Since both shape and energy position of the thin-film samples' satellite peaks perfectly match that of the $NiFe_2O_4$ bulk spectrum, we conclude that the Fe^{3+} cations occupy the bulk lattice sites, without any sign for a cationic inversion from the inverse to the normal spinel structure in the binding energy resolution limit of the performed HAXPES experiment.

In summary, both the Ni $2p$ and Fe $2p$ spectra are comparable to the spectrum of bulk material for all film thicknesses and reveal that the chemical composition of the bulk material is well reproduced in the ultrathin $NiFe_2O_4$ films. The Fe $2p_{3/2}$ satellite gives no hint for a cationic inversion in ultrathin $NiFe_2O_4$. In order to rule out also any smaller effect, we investigate the spatial cationic distribution by further spectroscopic means.

C. XANES

To gain precise information on the spatial cationic distribution in the $NiFe_2O_4$ thin films, we recorded XANES spectra of the Fe and Ni K edge. Since the fine structure above the absorption edge is dominated by multiple scattering with the surrounding atoms of the investigated cation species, XANES is very sensitive to the distribution of the oxygen anions around the cation. Thus, a cationic inversion—for which the local site occupancy changes from tetrahedral to octahedral, or vice versa—considerably modifies the shape of the spectral fine structure.

The absorption spectra of the $NiFe_2O_4$ film samples are recorded by fluorescence yield; thus, the measured data probe the bulk-like film properties.

Figure 5(b) shows the XANES spectra of the Fe K edge for $NiFe_2O_4$ films down to 2 nm and a bulk material reference spectrum. All spectra show a pre-edge feature at 7111 eV, which in the case of the spinel structure is observable for cations in a T_d symmetry only. While the main absorption line is caused by a dipole transition from the $1s$ to the empty $4p$ orbital, the pre-edge structures in transition-metal oxides are assigned to quadrupole transitions to the empty $3d$ states and thus are only very weak [35]. If the inversion symmetry of the transition-metal cation is broken, the local $3d$ and $4p$ wave functions of the cation hybridize, and in turn dipole transitions into this orbital become allowed, leading to an increased weight of the pre-edge feature. In the spinel structure a broken symmetry is given for cations on T_d sites, but not on O_h sites.

XANES studies of the Fe K edge of various spinels clearly show a sharp pre-edge for all materials exhibiting the inverse spinel structure, where Fe cations are situated on T_d sites. In contrast, the spectra of compounds featuring the normal spinel structure, in which Fe cations solely occupy O_h sites, only show a weak broad feature [34]. In Fig. 5(b), this is exemplarily shown by an XANES reference spectrum of the normal spinel $ZnFe_2O_4$ (reproduced from Ref. [34]).

The normalized pre-edge intensity can be quantitatively correlated to the local site symmetry of the investigated cation species [36]. By monitoring the Fe K edge pre-edge intensity of the $NiFe_2O_4$ samples, no intensity changes are resolvable between the various film thicknesses and also not in comparison to the bulk reference sample. We thus can conclude once more that the ultrathin films do not undergo a cationic

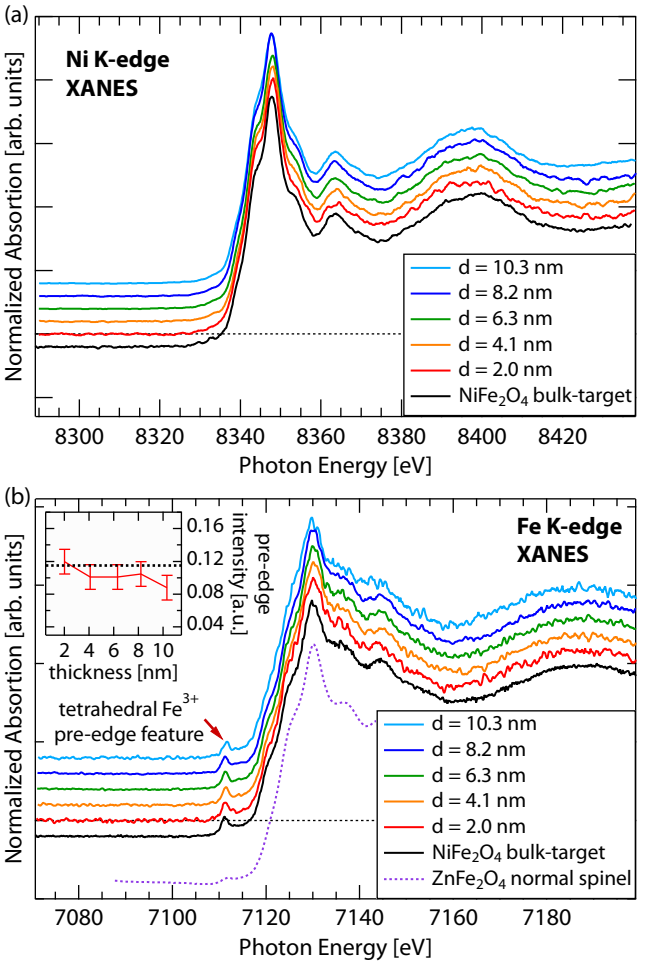

FIG. 5. (Color online) XANES spectra of (a) the Ni K edge and (b) the Fe K edge from $NiFe_2O_4$ films with varying film thickness. For comparison a Fe K edge spectrum of zinc ferrite, which exhibits the normal spinel structure, is plotted (reproduced from Ref. [34]). The inset in (b) shows the integrated spectral weight of the Fe K edge pre-edge feature in dependence of the film thickness, where the dotted line represents the bulk value.

inversion but remain in the bulk-like cationic distribution of the inverse spinel lattice. This is supported by the Ni K edge spectra [Fig. 5(a)], which also show no sign of an emerging pre-edge feature, characteristic for Ni cations on T_d sites.

Focusing on the main Fe K edge in Fig. 5(b), a chemical shift is expected for valency changes. A shift of about 5 eV between Fe^{2+} and Fe^{3+} for octahedrally coordinated iron oxides was observed previously [37]. A comparison of XANES spectra from bulk Fe_3O_4 with $NiFe_2O_4$, for which Fe^{2+} cations are replaced by Ni^{2+}, reveals a chemical shift of about 3 eV, which has been explained by the missing Fe^{2+} ions [38]. This energy shift has also been observed in other ferrites, where the Fe^{2+} cations are substituted by a different cation species [34]. In all cases, the Fe K edge of the Fe^{2+} compounds was situated at lower binding energies. In our case, we observe no chemical shift of the main edge across all film thicknesses, thus again supporting that no modification in the oxidation state of the Fe cations occurs, fully consistent with our HAXPES results.

The results of this in-depth XANES pre-edge analysis clearly reveal that $NiFe_2O_4$ films grow in the inverse spinel structure independent of their film thickness. Moreover, the position of the main K edges confirms that the Fe and Ni cations in all samples are present in a bulk-like valency for all film thicknesses.

D. XMCD

In a last step, we analyze the XMCD asymmetry signal to quantitatively determine the cationic distribution across the spinel lattice sites. The XMCD asymmetry spectra are element specific and sensitively influenced by the valency, the local lattice site symmetry, and the magnetic ordering of the investigated cation species. The spectral details reflect the superposition of cations occupying T_d or O_h sites with either divalent or trivalent valency, respectively. Hereby, each configuration has its own characteristic magnetic circular dichroism (MCD) spectrum, which serves as a fingerprint for the certain atomic and geometric configuration. We thus modeled those four XMCD spectra, which allowed us to fit them as a linear combination to the experimental data and to quantify the fraction of each configuration.

We investigated XMCD asymmetry spectra of the Fe $L_{2,3}$ edge to identify any changes in the distribution of Fe cations between T_d and O_h lattice sites for $NiFe_2O_4$ films with varying thickness. Site- and valency-specific Fe $L_{2,3}$-edge XMCD spectra were computed by ligand field multiplet (LFM) calculations utilizing the software CTM4XAS [18] and are presented in Fig. 6(b). Due to the antiferromagnetic alignment of the cation spins between T_d and O_h sites, their asymmetry signals are of opposite sign. Consequently, these signals mainly cancel out in the observable sum asymmetry signal, leaving the resulting difference spectrum extremely sensitive to subtle changes in the cationic distribution.

Figure 6(a) exemplarily shows the MCD spectrum of the Fe $L_{2,3}$ edge for the 2-nm-thick $NiFe_2O_4$ film with the corresponding fit. The L_3 edge exhibits a pronounced $-/+/-$ asymmetry structure, caused by the antiparallel-oriented Fe moments. The positive (+) peak at 709.7 eV (II) is dominated by tetrahedral Fe^{3+} and the high-energy negative ($-$) peak at 710.5 eV (III) by octahedral Fe^{3+} cations. The first negative peak at 708.5 eV (I) cannot be directly associated with the presence of Fe^{2+} cations, because it appears both in the reference data of bulk $NiFe_2O_4$ [22] and in the model spectrum for Fe^{3+} cations. Yet, the first peak is larger in comparison to the reference data, thus indicating the presence of a fraction of Fe^{2+} cations at the surface, which is determined within $\approx 2\%$ from the model fit.

However, the result gives no indication for a cationic inversion of the film, which would result in a decrease of the positive peak (II) and strong enhancement of the high-energy negative peak (III). These results are also observed for all other investigated $NiFe_2O_4$ film thicknesses, which give no clue for an increased octahedral Fe^{3+} fraction, as would be characteristic for a cationic inversion to the normal spinel structure. This finding is in perfect agreement with electronic structure calculations, which find the fully inverse spinel lattice to be the ground state of bulk $NiFe_2O_4$ [39].

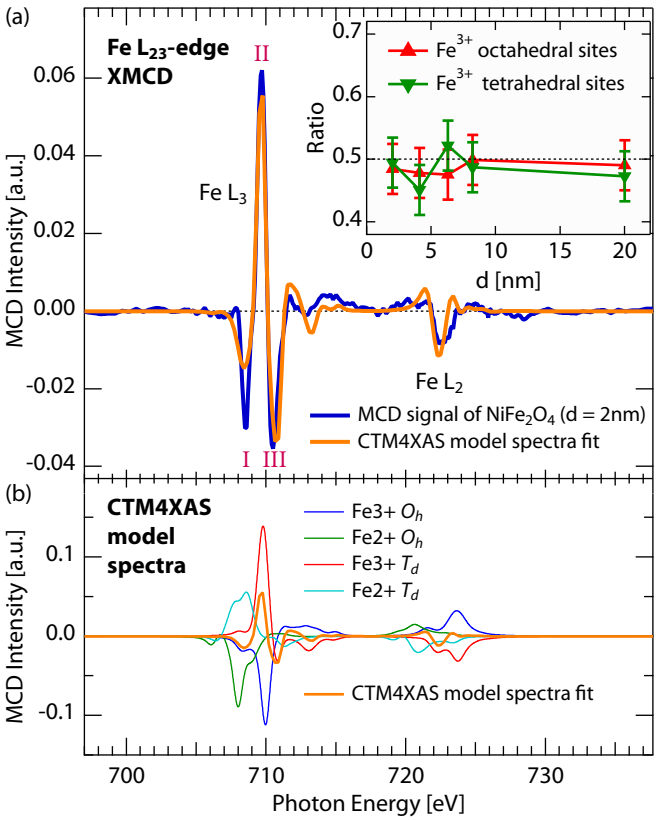

FIG. 6. (Color online) Experimental XMCD spectrum from the Fe $L_{2,3}$ edge of the 2-nm-thick $NiFe_2O_4$ film and the corresponding fit. The resulting lattice site occupancy for various film thicknesses is depicted in the inset.

Since the XMCD spectra are recorded in TEY mode, the experiment probes the uppermost 2–3 nm of material. Complemented by the bulk-sensitive HAXPES and XANES techniques, the analysis yields a consistent picture of the stoichiometry, valency, and cationic distribution of the $NiFe_2O_4$ thin films. In particular, we find that the cationic site occupancy always belongs to that of an inverse spinel lattice; this result is found both at the $NiFe_2O_4$ surface and in the bulk volume. This striking consistency provides clear evidence for the absence of a cationic inversion in $NiFe_2O_4$ in the crossover to the ultrathin-film limit and thus rules out this mechanism as the origin of the observed enhanced M_S in ultrathin $NiFe_2O_4$ films.

IV. SUMMARY

In summary, we have investigated single-crystalline $NiFe_2O_4$ thin films grown cube-on-cube on Nb-doped $SrTiO_3$ (001) substrates, with thicknesses scaling down from 20 to 2 nm. In this crossover to the ultrathin-film limit, we focused on the impact of reduced dimensionality on the structural, electronic, and magnetic $NiFe_2O_4$ properties. Foremost, we observed an enhanced saturation magnetization M_S in ultrathin $NiFe_2O_4$ films. Despite the substrate-induced compressive in-plane strain, a reduced out-of-plane $NiFe_2O_4$ lattice constant is found, implying that a reduction of the unit cell volume is energetically favorable. In order to investigate the

cationic distribution in the $NiFe_2O_4$ thin films, complementary bulk- and surface-sensitive analyses using HAXPES, XANES, and XMCD spectroscopy techniques have been performed, and special attention was paid to the element-specific cation valencies and coordinations. We find a bulk-like inverse spinel structure present in all samples—independent of the $NiFe_2O_4$ film thickness. Thereby, our results consistently reveal the absence of a cationic inversion from the inverse to the normal spinel structure, as was so far held responsible for an enhanced M_S in ultrathin spinels. From our experimental results we find an auxetic behavior, i.e., a structural unit cell reduction, in ultrathin $NiFe_2O_4$ films. Further experiments and theoretical calculations will further elucidate these possibly correlating physical mechanisms.

ACKNOWLEDGMENTS

We acknowledge experimental support during beam times by B. Zijlstra and C. Caspers. We thank R. Dittmann for providing the PLD setup and the JCNS-2 for providing the MPMS at FZJ. This work has been funded by the Helmholtz Association under Grant No. HGF-NG-811.

[1] H. Y. Hwang, Y. Iwasa, M. Kawasaki, B. Keimer, N. Nagaosa, and Y. Tokura, Nat. Mater. **11**, 103 (2012).
[2] R. Seshadri, S. L. Brock, A. Ramirez, M. Subramanian, and M. E. Thompson, MRS Bull. **37**, 682 (2012).
[3] G.-X. Miao, M. Müller, and J. S. Moodera, Phys. Rev. Lett. **102**, 076601 (2009).
[4] M. Müller, M. Luysberg, and C. M. Schneider, Appl. Phys. Lett. **98**, 142503 (2011).
[5] C. Caspers, M. Müller, A. X. Gray, A. M. Kaiser, A. Gloskovskii, C. S. Fadley, W. Drube, and C. M. Schneider, Phys. Rev. B **84**, 205217 (2011).
[6] C. Caspers, A. Gloskovskij, W. Drube, C. M. Schneider, and M. Müller, Phys. Rev. B **88**, 245302 (2013).
[7] V. A. M. Brabers, in *Handbook of Magnetic Materials* (Elsevier, Amsterdam, 1995), pp. 189–324.
[8] J. X. Ma, D. Mazumdar, G. Kim, H. Sato, N. Z. Bao, and A. Gupta, J. Appl. Phys. **108**, 063917 (2010).
[9] M. Hoppe, M. Gorgoi, C. M. Schneider, and M. Müller, IEEE Trans. Magn. **50**, 2506204 (2014).
[10] U. Lüders, M. Bibes, J.-F. Bobo, M. Cantoni, R. Bertacco, and J. Fontcuberta, Phys. Rev. B **71**, 134419 (2005).
[11] S. Venzke, R. B. van Dover, J. M. Phillips, E. M. Gyorgy, T. Siegrist, C.-H. Chen, D. Werder, R. M. Fleming, R. J. Felder, E. Coleman, and R. Opila, J. Mater. Res. **11**, 1187 (1996).
[12] D. Fritsch and C. Ederer, Appl. Phys. Lett. **99**, 081916 (2011).
[13] G. Koster, B. L. Kropman, G. J. H. M. Rijnders, D. H. A. Blank, and H. Rogalla, Appl. Phys. Lett. **73**, 2920 (1998).
[14] M. Gorgoi, S. Svensson, F. Schäfers, G. Öhrwall, M. Mertin, P. Bressler, O. Karis, H. Siegbahn, A. Sandell, H. Rensmo, W. Doherty, C. Jung, W. Braun, and W. Eberhardt, Nucl. Instrum. Methods Phys. Res., Sect. A **601**, 48 (2009).
[15] W. Drube, Nucl. Instrum. Methods Phys. Res., Sect. A **547**, 87 (2005).
[16] C. J. Powell and A. Jablonski, Nucl. Instrum. Methods Phys. Res., Sect. A **601**, 54 (2009).
[17] Wolfgang S. M. Werner, Werner Smekal, and Cedric J. Powell, *NIST Database for the Simulation of Electron Spectra for Surface Analysis (SESSA), Version 1.3* (National Institute of Standards and Technology, Gaithersburg, MD, 2011).
[18] E. Stavitski and F. M. de Groot, Micron **41**, 687 (2010).
[19] B. Thole, G. van der Laan, and P. Butler, Chem. Phys. Lett. **149**, 295 (1988).
[20] H. Ogasawara, A. Kotani, K. Okada, and B. T. Thole, Phys. Rev. B **43**, 854 (1991).
[21] H. Ogasawara, A. Kotani, R. Potze, G. A. Sawatzky, and B. T. Thole, Phys. Rev. B **44**, 5465 (1991).
[22] R. A. D. Pattrick, G. van der Laan, C. M. B. Henderson, P. Kuiper, E. Dudzik, and D. J. Vaughan, Eur. J. Mineral. **14**, 1095 (2002).
[23] M. Foerster, M. Iliev, N. Dix, X. Martí, M. Barchuk, F. Sánchez, and J. Fontcuberta, Adv. Funct. Mater. **22**, 4344 (2012).
[24] J. A. Moyer, C. A. F. Vaz, D. P. Kumah, D. A. Arena, and V. E. Henrich, Phys. Rev. B **86**, 174404 (2012).
[25] D. T. Margulies, F. T. Parker, M. L. Rudee, F. E. Spada, J. N. Chapman, P. R. Aitchison, and A. E. Berkowitz, Phys. Rev. Lett. **79**, 5162 (1997).
[26] F. Rigato, J. Geshev, V. Skumryev, and J. Fontcuberta, J. Appl. Phys. **106**, 113924 (2009).
[27] M. Foerster, J. M. Rebled, S. Estradé, F. Sánchez, F. Peiró, and J. Fontcuberta, Phys. Rev. B **84**, 144422 (2011).
[28] S. K. Arora, H.-C. Wu, R. J. Choudhary, I. V. Shvets, O. N. Mryasov, H. Yao, and W. Y. Ching, Phys. Rev. B **77**, 134443 (2008).
[29] J. Orna, P. A. Algarabel, L. Morellón, J. A. Pardo, J. M. de Teresa, R. López Antón, F. Bartolomé, L. M. García, J. Bartolomé, J. C. Cezar, and A. Wildes, Phys. Rev. B **81**, 144420 (2010).
[30] D. Alders, F. C. Voogt, T. Hibma, and G. A. Sawatzky, Phys. Rev. B **54**, 7716 (1996).
[31] T. Fujii, F. M. F. de Groot, G. A. Sawatzky, F. C. Voogt, T. Hibma, and K. Okada, Phys. Rev. B **59**, 3195 (1999).
[32] M. A. van Veenendaal and G. A. Sawatzky, Phys. Rev. Lett. **70**, 2459 (1993).
[33] M. C. Biesinger, B. P. Payne, A. P. Grosvenor, L. W. M. Lau, A. R. Gerson, and R. S. C. Smart, Appl. Surf. Sci. **257**, 2717 (2011).
[34] K. Matsumoto, F. Saito, T. Toyoda, K. Ohkubo, K. Yamawaki, T. Mori, K. Hirano, M. Tanaka, and S. Sasaki, Jpn. J. Appl. Phys. **39**, 6089 (2000).
[35] F. d. Groot, G. Vankó, and P. Glatzel, J. Phys.: Condens. Matter **21**, 104207 (2009).
[36] M. Wilke, F. Farges, P.-E. Petit, G. E. Brown Jr., and F. Martin, Am. Mineral. **86**, 714 (2001).
[37] S. Sasaki, Rev. Sci. Instrum. **66**, 1573 (1995).
[38] F. Saito, T. Toyoda, T. Mori, M. Tanaka, K. Hirano, and S. Sasaki, Phys. B **270**, 35 (1999).
[39] Z. Szotek, W. M. Temmerman, D. Ködderitzsch, A. Svane, L. Petit, and H. Winter, Phys. Rev. B **74**, 174431 (2006).